



Title	Temperature and Confining Pressure Effects on the Permeability of Fractured Rocks
Author(s)	Alam, A. K. M. Badrul; Fujii, Yoshiaki; Kaneko, Katsuhiko; Aramaki, Noritaka
Citation	資源・素材2015（松山）企画発表・一般発表講演集, 2015, 3411
Issue Date	2015-09-08
Doc URL	http://hdl.handle.net/2115/62719
Type	proceedings
Note	資源・素材2015（松山）平成27年度資源・素材関係学協会合同秋季大会 , 2015年9月8日～10日, 愛媛大学, 松山市
File Information	MMIJ2015Matsuyama3411.pdf



[Instructions for use](#)

企画講演

YARO13 温度－熱く研究, クールに考察－

2015年9月10日(木) 13:00 ~ 14:20 第4会場 (EL24)

[3411] 岩石の透水性に及ぼす温度および封圧の影響 Temperature and confining pressure effects on the permeability of fractured rocks

○A.K.M. Badrul Alam¹, Fujii Yoshiaki², Kaneko Katsuhiko¹, Aramaki Noritaka¹ (1.Northern Advancement Center for Science and Technology, 2.Hokkaido University)

キーワード : fractured rocks, permeability, temperature, confining pressure

Permeability was measured in triaxial compression condition under confining pressures of 1–15 MPa at 295 K and 353 K on Shikotsu welded tuff, Kimachi sandstone, and Inada granite. At 295 K, the post-compression permeability of Shikotsu welded tuff became smaller than that before axial compression. The permeability of Kimachi sandstone was higher than that before axial compression under low confining pressures, but lower under higher confining pressures. On the other hand, the post-compression permeability of Inada granite was higher than that before axial compression regardless of the confining pressure values. At 353 K, the post-compression permeability was lower than at 295 K for all the rock types but not so obvious for Kimachi sandstone. Influence of confining pressure was less for Shikotsu welded tuff but more apparently for Inada granite than at 295 K. The reasons behind the permeability changes are discussed.

1. Introduction

Stress redistribution and permeability changes within Excavation-disturbed Zones (EdZs) and Excavation-Damaged Zones (EDZs) [Sato et al., 2000; Fujii et al., 2011; Tsang et al., 2005]. The confining pressure in an EDZ can be either low in the vicinity of the opening (EDZ 2 in Fig. 1a) or relatively high (EDZ 1 in Fig. 1a). The temperature change of rock masses can be induced by human activity or natural processes. In particular, in radioactive waste repositories which are needed to be maintained for long periods even after closure, the temperature rises due to the heat generated by decay after the waste has been emplaced and the opening has been backfilled. The confining pressure increases due to swelling of the backfill. The axial stress increases due to thermal stress caused by the temperature gradient in the surrounding rock mass and swelling pressure from the backfill (Fig. 1C (3)). The thermal stress decreases after the decay heat disappears, but the confining pressure remains unchanged (Fig. 1C (4)). These temperature and confining pressure changes could influence the permeability situation in the vicinity of the disposal site. In this experimental research, the temperature and confining pressure effects on the permeability of rocks was investigated as THM processes under compression.

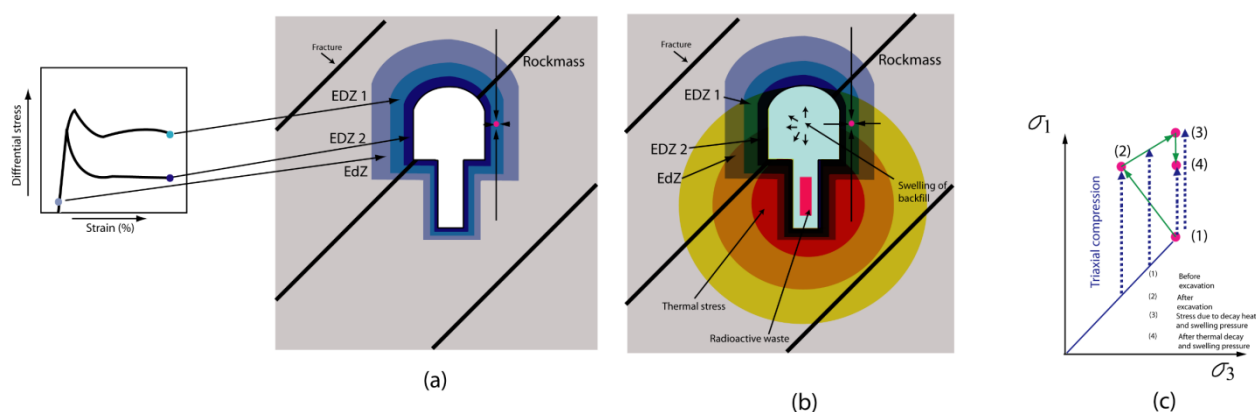


Figure 1 Schematic diagram of the EdZ, EDZs and fractures around an underground opening (a), thermal stress from radioactive waste and swelling pressure from backfill (b), and, comparison of comparison of the stress paths of a radioactive disposal site and that adopted in the triaxial compression tests (c).

2. Materials and methods

2.1 Rock types

Rock masses consisting of different types of rock are being considered for radioactive waste disposal site, including crystalline and clastic rocks, clay, tuff, rock salt, etc. In this research, Inada granite, Kimachi sandstone and Shikotsu welded tuff were chosen for consideration of the effects of temperature and confining pressure as THM processes on a wide range of physical properties of rocks.

2.2 Experimental procedure

The undisturbed rock blocks were collected and the specimens were prepared from the blocks of cylindrical cores that had a diameter of around 30 mm and a length of 60 mm. Specimens were fully saturated in de-ionized water in a water-submergible vacuum jar. After a pair of stainless steel endpieces was attached and two cross-type strain gauges were glued to the specimen. The sample was covered by a heat-shrinkable tube and was submerged in de-ionized water for 24 h. Each sample was inserted into the ultra compact triaxial cell (Fig. 2a) having a band-type heater with a controller (Fig. 2). Then, axial stress and confining pressure were applied. The triaxial tests were carried out under 1–15 MPa of confining pressure at 295 or 353 K. After reaching the target consolidation pressure, the sample was held in this state for 24 h. The time for consolidation to stabilize the initial time-dependent deformation was long enough as the volumetric deformation was stabilized within 20 h for all rocks.

After consolidation, a constant strain rate (10^{-5} s^{-1} , i.e., 0.036 mm/min)-controlled compression was applied measuring permeability. The permeability of the Shikotsu welded tuff was measured by the constant flow method and the permeability of Kimachi sandstone and Inada granite was measured by the transient-pulse method [Alam et al., 2014] considering the approximate solution by Brace et al. [Brace et al., 1968].

During the experiment, the load, stroke, pore pressure, axial strain, lateral strain, confining pressure, and flow rate were recorded on a data logger at a sampling interval of 10 s.

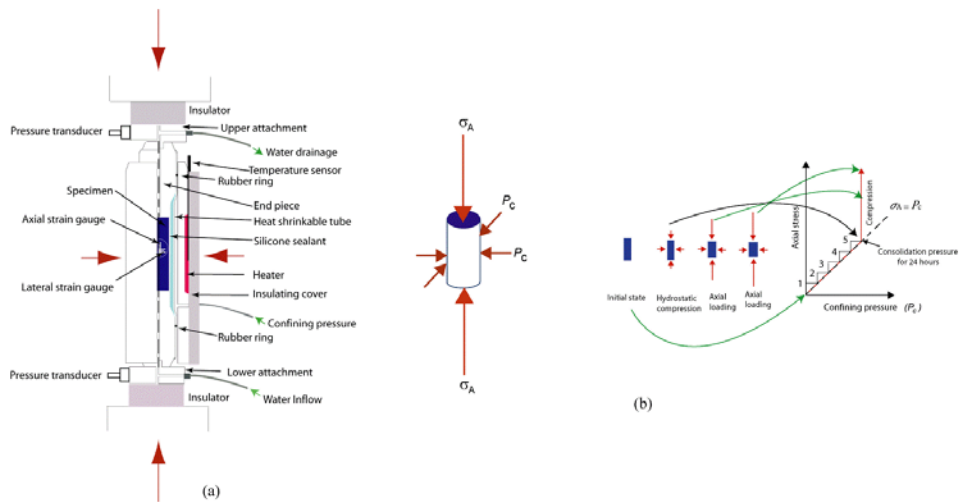


Figure 2 The ultra compact triaxial cell with a heater and the experimental loading path. (a) The triaxial cell with the arrangement to apply confining pressure and temperature, (b) The loading path of the experiment.

2.3 Micro- and macrostructure analysis

Microstructures (pore characteristics of Shikotsu welded tuff, thickness of the cementing material for Kimachi sandstone, and crack characteristics of Inada granite) by thin section images and macrostructures (number, orientation, and geometry of the rupture planes and fractures) by using X-ray CT images of the post-compression specimens were analyzed. The thin-section images of the blue-resin-impregnated specimens were viewed at a resolution of $8.8 \times 8.8 \mu\text{m}$. The macrostructures of the post-compression specimens were observed using a microfocus X-ray-computed tomography (CT) scanner with a $37 \times 37 \times 80 \mu\text{m}$ resolution.

3. Results

3.1 The effects of deformation and failure on permeability under compression

The permeability behavior during deformation and the behavior with volumetric strain during axial compression are in Fig. 3, and Fig. 4 respectively. The permeability values are shown in Fig. 5 with the regression lines to show the upper and lower limits of 95% confidence interval which were drawn twice the standard deviation above and below the regression line in Fig. 5. Three words are being used to indicate the influence of temperature considering the regression line. The word "lower" is used when the intervals for 295 K and 353 K are not overlapped, or overlapped roughly less than 30% total area. When they are overlapped roughly 30 - 60% total area then the word "slightly" whereas "no obvious/almost the same" if the overlapping is roughly more than 60% are being used.

In case of Shikotsu welded tuff, the permeability during deformation and failure under compression at 295 K, as well as at 353 K, monotonically decreased even after the specimen began to expand (Figs. 3 and 4). The post-compression permeability decreased with the confining pressure at 295 K, but the permeability at 353 K was almost the same in the all confining pressures and as low as that under 15 MPa CP at 295 K (Fig. 5 i). The flow velocity per unit pore pressure gradient, which was calculated by substituting the permeability of rock and the viscosity of water into the Darcy's law, was slightly lower at 1 MPa CP. It was almost the same at 15 MPa CP as the values at 295 K (Fig. 5j). The permeability change (Fig. 6) was calculated from the permeability after 24 hours of consolidation (K_{con}) and the post-compression permeability (K_{com}) as

$$K_{\text{change}} = ((K_{\text{com}} - K_{\text{con}}) / K_{\text{con}}) / 100. \quad (1)$$

The change in permeability showed that the decrease became greater with increasing confining pressure from -3.05% to -92.12% at 295 K (Fig. 6a). No confining-pressure dependency was observed at 353 K (-84.21% to -93.93%).

For Kimachi sandstone, the permeability during deformation and failure under compression at 295 K, as well as at 353 K, first decreased, then began to increase before the specimen began to expand. It continued to increase showing peak stress and was nearly stabilized in the residual strength state (Figs. 3 and 4). The stress relaxations occurred since the platen was stopped during permeability measurement by transient pulse method. The minimum permeability declined with the confining pressure, and no obvious difference was apparent between 295 and 353 K (Fig. 5a). The flow velocity per unit pore pressure gradient was almost the same at 353 K (Fig. 5b). The post-compression permeability declined with the confining pressure, and the permeability at 353 K was slightly lower (Fig. 5e). However, the flow velocity per unit pore pressure gradient at 353 K was almost the same (Fig. 5f). At 295 K, the permeability

became higher for failure under low confining pressure, and the permeability change (Equation 1) was as high as 179.0% (Fig. 6b). The permeability showed a decrease under high confining pressure by as much as -47.0%. The permeability decreased at 353 K, except for 1 MPa CP. The amount of the decrease was almost the same as that at 295 K.

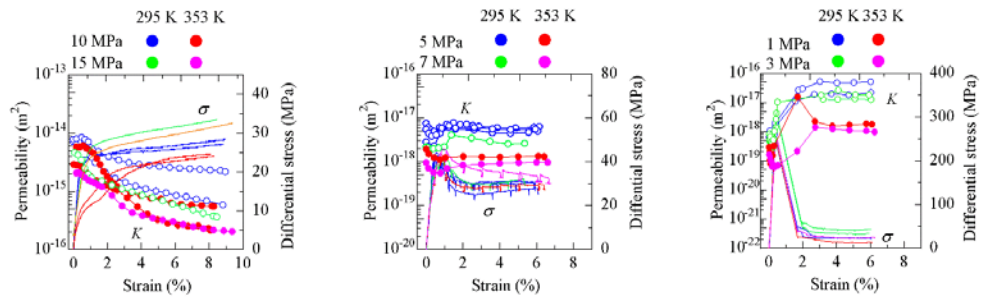


Figure 3 Examples of stress-strain curves and evolution of permeability due to deformation and failure. The axial strain here is defined as change in strain during axial compression.

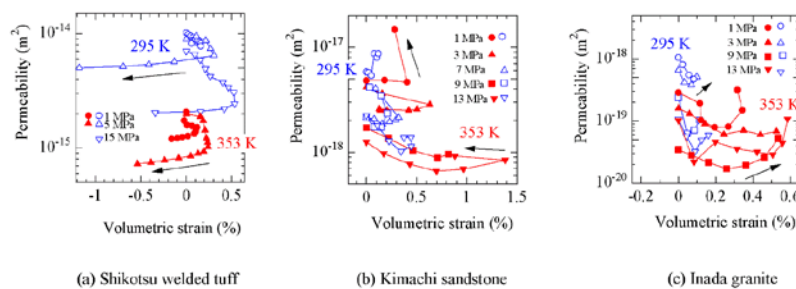


Figure 4 Permeability behavior with volumetric strain during axial compression. Most of the curves are not to the residual strength since the strain gages often broke during axial compression.

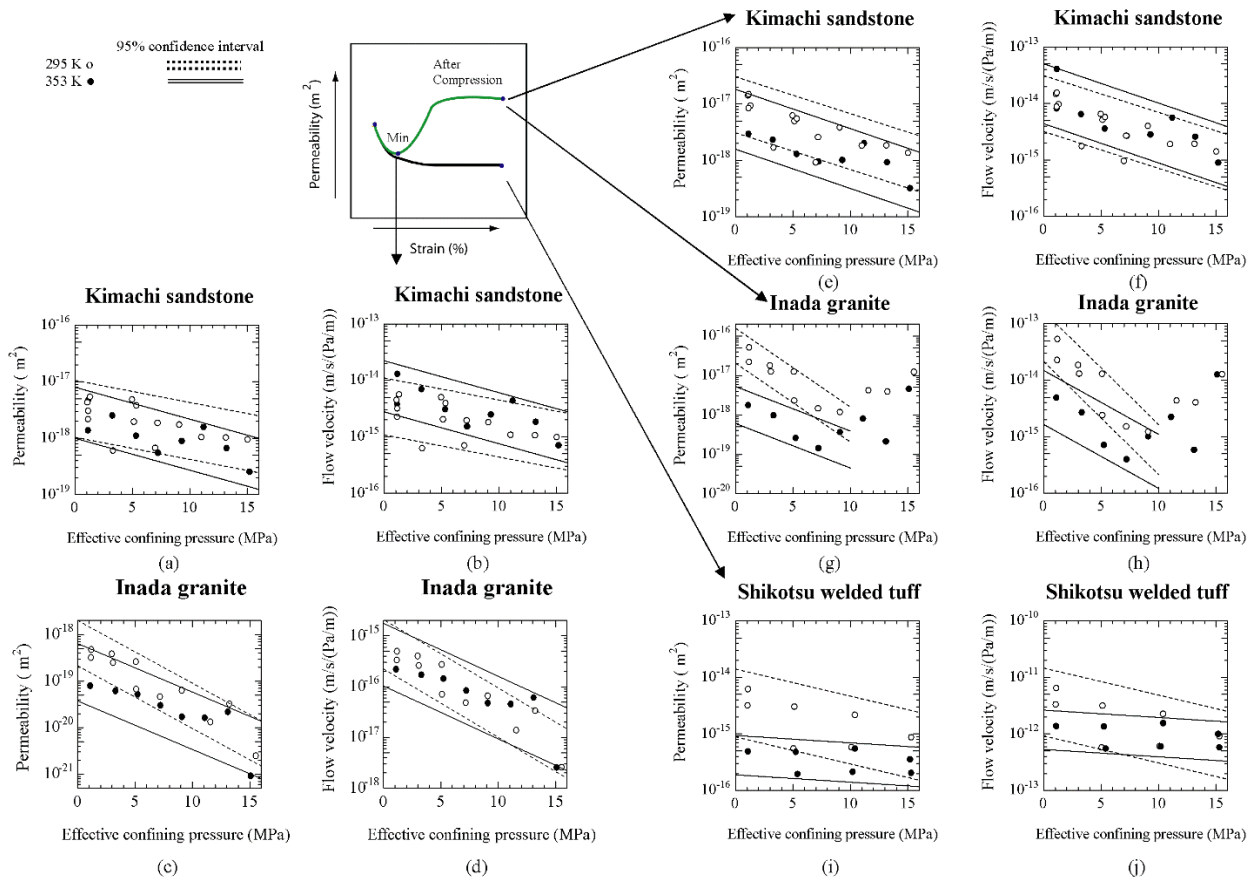


Figure 5 Minimum and post-compression permeability and flow velocity per unit pore pressure gradient.

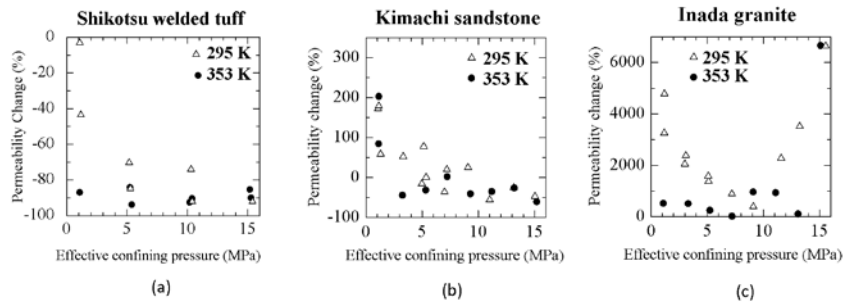


Figure 6 Temperature–confining–pressure coupling effect on the permeability change from pre- to post-compression.

The permeability of Inada granite during deformation and failure under compression at 295 K, as well as at 353 K, behaved in a manner similar to that of Kimachi sandstone. The minimum permeability declined with the confining pressure at both 295 and 353 K, although the permeability at 353 K was slightly lower than at 295 K (Fig. 5c). The flow velocity per unit pore pressure gradient at 353 K was almost the same as at 295 K (Fig. 5d). The post-compression permeability declined with the confining pressure up to 7 MPa CP at 353 K or 9 MPa CP at 295 K, and then increased again. The permeability (Fig. 5g) and flow velocity per unit pore pressure gradient (Fig. 5h) at 353 K were lower than those at 295 K up to 10 MPa CP. At 295 K, the permeability increased with failure, and the permeability change became as great as 4780% (Fig. 6c). The ratio decreased to 394% with confining pressure until it attained 9 MPa CP, and then increased again to 6640% at 15 MPa CP. At 353 K, the permeability increase was nearly independent of the confining pressure, except for 15 MPa CP, and was as small as the smallest increase at 295 K (Fig. 6c).

3.2 The changes of rock structures in post compression specimens

In the case of Shikotsu welded tuff, in the post compression specimens a main rupture plane with sub-rupture planes and several fractures appeared in the CT image for 1 MPa CP at 295 K (Fig. 7a), whereas only one main rupture plane appeared at 353 K (Fig. 7b). The porosity near the rupture plane was higher than the porosity far-removed from it (Fig. 7i). The porosity far-removed from the rupture plane at 353 K was 10.0% less than at 295 K. The rupture plane was absent in 15 MPa cases (Fig. 7e and f), and their porosity at 353 K was less than at 295 K by 4.63% (Fig. 7i). The number of pores with an equivalent diameter of 0.06 mm - 0.18 mm at 353 K was lower than that at 295 K at 1 MPa CP far from the rupture plane (Fig. 8a). Pores with a smaller equivalent diameter of 0.06 mm were dominant at 353 K, but pores with a diameter of 0.10 mm were dominant under 15 MPa CP at 295 K (Fig. 8b). The pores with an aspect ratio of 0.50 decreased more at 353 K than that at 295 K under 1 MPa CP and far from the rupture plane (Fig. 8c). The aspect ratio frequency of 0.35 was dominant at 353 K, whereas a frequency of 0.45 was dominant at 295 K under 15 MPa CP (Fig. 8d). These pore properties suggest that pore collapse at 353 K under 1 MPa CP and far from the rupture plane and at both 295 K and 353 K under 15 MPa CP.

In the case of Kimachi sandstone, main and sub-rupture planes occurred as well as several fractures in the CT image for 1 MPa CP at 295 K (Fig. 9a) in the post compression specimen. However, only one main rupture plane and one sub-rupture plane appeared under 1 MPa CP at 353 K (Fig. 9b). The average thickness of the cementing material was approximately 0.20 mm at both temperatures (Fig. 9h). There were two rupture planes under 3 MPa CP at 295 K (Fig. 9c). On the other hand, only one rupture plane was observed at both 295 K and 353 K (Fig. 9h) at 353 K (Fig. 9d). The rupture planes were absent for the 15 MPa CP cases (Fig. 9e and f). The thickness of cementing materials was approximately 0.15 mm.

In the case of Inada granite, one distinct, thick main rupture plane with many sub-rupture planes and fractures appeared in the CT image for 1 MPa CP at 295 K (Fig. 10a) in the post compression specimen. The rupture plane comprised the network of microcracks that were observed in the thin-section image. Axial cracks that had propagated from biotite also were observed (Fig. 10c). One main thin rupture plane was formed under 7 MPa CP without axial cracks from biotite (Fig. 10f) at 295 K. In the cases of 1 and 7 MPa CP at 353 K (Fig. 10b and g), one main thin rupture plane and one sub-rupture plane were observed with elongated biotite grains along the rupture planes in the thin-section images (Fig. 10d and e). For 15 MPa CP, two main rupture planes formed at 295 K (Fig. 10i). One rupture plane with sub-rupture planes and many fractures appeared at 353 K (Fig. 10h).

4. Discussion

In the post-compression state, the largest permeability decrease was achieved for Shikotsu welded tuff at 15 MPa CP at 295 K. The

decrease was even greater for 1 MPa CP at 353 K (Fig. 6a) due to the low porosity of the matrix (Fig. 7i). The main cause of this phenomenon was enhanced pore collapse by temperature–confining-pressure coupling, as the number of pores declined by confining pressure or temperature (Fig. 8 a, c).

The post-compression permeability of Kimachi sandstone at 353 K (Fig. 5e) was slightly lower than at 295 K, because of the relatively smaller thickness of cementing materials. The decrease in thickness was mainly caused by plastic deformation since the clay minerals are weaker than the mineral grains and the yielded clay deformation is plastic and may include some viscous deformation. The plastic deformation was enhanced mainly by confining pressure. For example, the greatest permeability decrease took place below 15 MPa CP at 353 K. The thickness of the cementing material was only 1.8% lower than that at 295 K, but was 23.8% lower than that under 1 MPa CP at 353 K (Fig. 9h).

The post-compression permeability of Inada granite at 353 K was also lower than at 295 K (Fig. 5g). This was due to the decrease in the number and thickness of sub-rupture planes and fractures, including the axial microcracks from biotite (Fig. 10), because of the enhancement of viscous deformation of unfailed mineral particles by thermal activation. The elongation of biotite particles along the rupture plane by temperature–confining pressure coupling (Fig. 10d and e) was another reason for the low permeability.

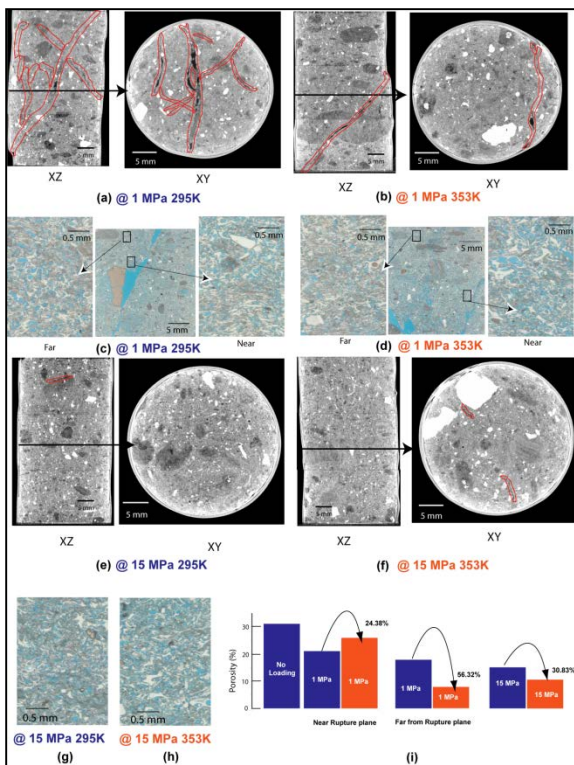


Figure 7 CT and thin-section images for post-compression specimens of Shikotsu welded tuff. (Red and blue areas represent fractured zones, and blue spots are pores in the images)

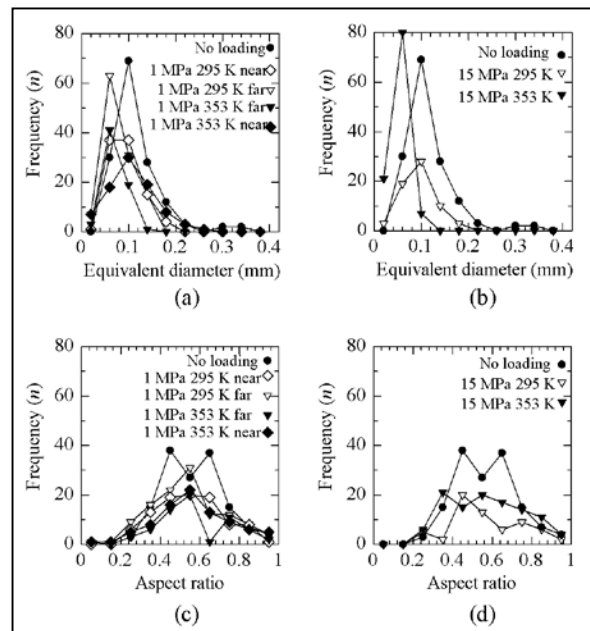


Figure 8 Thin sectional image analysis of the blue resin impregnated thin sectional images of the post compression specimen. (a) equivalent diameter at 1 MPa CP, (b) equivalent diameter at 15 MPa CP, (c) Aspect ratio at 1 MPa CP, (d) Aspect ratio at 15 MPa.

5. Conclusions

For the all rock types, the permeability at 353 K was lower than at 295 K, and the influence of the confining pressure was less at 353 K than at 295 K of the post compression specimens that were fractured. The above temperature effects were observed apparently for Inada granite, only the latter effect was apparent for Shikotsu welded tuff, and they were not so obvious for Kimachi sandstone. The principal mechanisms causing the permeability decrease were enhancement of pore collapse for the Shikotsu welded tuff, plastic deformation of the cementing material for Kimachi sandstone, and viscous deformation of mineral particles for Inada granite by thermal activation.

The flow velocity of the fractured specimens with the unit pore pressure gradient at 353 K was slightly lower under low confining

pressures for the Shikotsu welded tuff, almost the same for the Kimachi sandstone, and less for Inada granite than the values at 295 K. These findings could be useful towards the optimum design of man-made caverns.

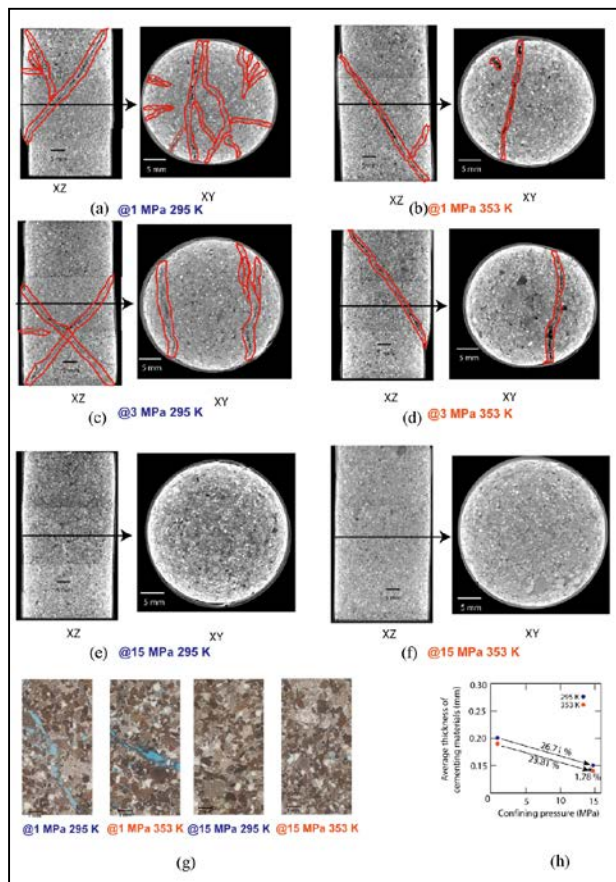


Figure 9 CT and thin-section images for post-compression specimens of Kimachi sandstone. (Red and blue areas in the images represent fractured zones)

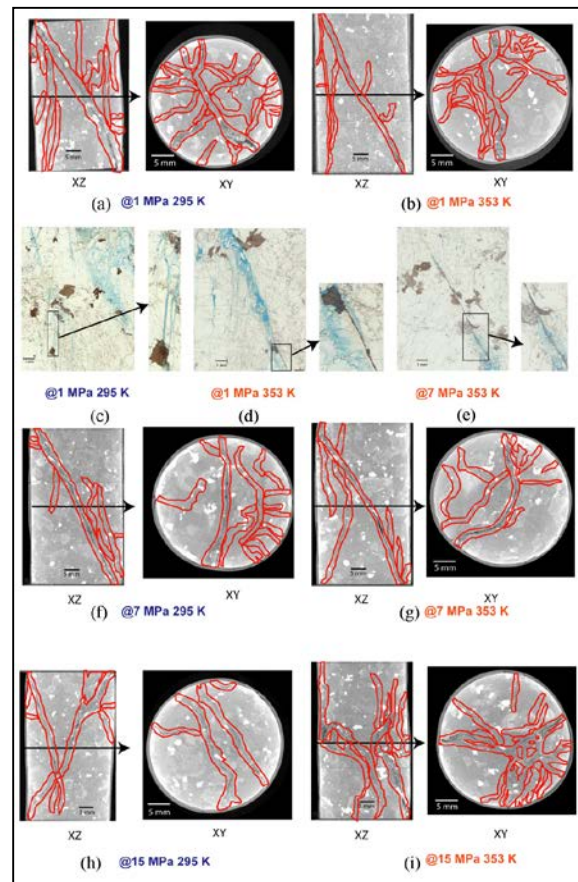


Figure 10 CT and thin-section images for post-compression specimens of Inada granite. (Red and blue areas in the images represent fractured zones)

Acknowledgments

This research work was partially supported by KAKENHI (22560804).

References

- 1) Sato, T., T. Kikuchi, and K. Sugihara, In-situ experiments on an excavation disturbed zone induced by mechanical excavation in neogene sedimentary rock at Tono mine, central Japan, Eng. Geol., Vol. 56, No. 1-2, pp. 97–108, 2000.
- 2) Fujii, Y., Y. Ishijima, Y. Ichihara, T. Kiyama, S. Kumakura, M. Takada, T. Sugawara, T. Narita, J. Kodama, M. Sawada, E. Nakata, Mechanical properties of abandoned and closed roadways in the Kushiro Coal Mine, Japan, Int. J. Rock Mech. Min. Sci., Vol. 48, pp. 585–596, 2011.
- 3) Tsang, C.-F., F. Bernier, C. Davies, Geohydromechanical processes in the excavation damaged zone in crystalline rock, rock salt, and indurated and plastic clays—in the context of radioactive waste disposal, Int. J. Rock Mech. Min. Sci., Vol. 42, pp. 109–125, 2005.
- 4) Alam, A.K.M. B., M. Niioka, Y. Fujii, D. Fukuda, and J. Kodama, Effect of confining pressure on the permeability of three rock types under compression, Int. J. Rock Mech. Min. Sci., Vol. 65, No. 1, pp. 49-61, 2014.
- 5) Brace, W.F., J.B. Walsh, and W.T. Frangos, Permeability of granite under high pressure, J. Geophys. Res., Vol. 73, pp. 2225–2236, 1968.